Analytical and Numerical Study of the Unstable Limit Cycles of Walking Droplets

by

Benjamin Kurzban

Submitted to the
Department of Mechanical Engineering
in Partial Fulfillment of the Requirements for the Degree of

Bachelor of Science in Mechanical Engineering

at the

Massachusetts Institute of Technology

May 2020

Signature of Author: _____

Department of Mechanical Engineering
May 8, 2020

Certified by: _____

Matthew Durey
Instructor of Mathematics
Thesis Supervisor

Accepted by: _____

Maria Yang
Professor of Mechanical Engineering
Undergraduate Officer

ANALYTICAL AND NUMERICAL STUDY OF THE UNSTABLE LIMIT CYCLES OF WALKING DROPLETS

BENJAMIN KURZBAN

ABSTRACT. Recent studies have shown that a vibrating fluid bath can support a bouncing droplet, generating a pilot wave which propels the droplet into horizontal motion. Walking droplets have been demonstrated not only to follow linear trajectories, but to exhibit a range of rich dynamical behavior, including tunneling, diffraction, and orbital quantization. Current theoretical models for the walking droplet system can be difficult to analyze. Here, by reducing the dimension of the bath, a simpler model has been derived and analyzed. We summarize this derivation, explore the stability of the system's dynamical states, and provide evidence of a previously unreported homoclinic bifurcation.

1. Introduction

The dynamics of droplets bouncing and self-propelling on the surface of a vertically vibrating fluid bath have been studied throughout the past decade. In such a system, as the droplet bounces on the bath it generates standing Faraday waves which affect its motion at future impacts. The longevity of these waves is determined by the vigor of the subcritical vibrational forcing, endowing the droplet with a memory of its prior trajectory. For "resonant walkers" (i.e. droplets whose vertical motion is in synchrony with the oscillation of the waves), Oza et al. [4] demonstrated that the resonant system may be time-averaged over one bouncing period, from which the droplet may be regarded as a continuous wave source, guided by its accompanying pilot wave. Using this assumption, they derived an integro-differential equation as a model for the trajectory of a walking droplet.

The dynamics of a free walker depends on its path memory: At short path memory (corresponding to weak vibrational forcing), the self-propulsion is steady, whereas chaotic random-walk-like motion arises when the influence of the walker's past trajectory is sufficiently pronounced for more vigorous forcing [3]. Couder et al. [2] have explored experimentally not only simple walkers, but also collisions and orbits of multiple such walkers. By subjecting the droplet to applied forces or boundaries, a range of more complex behavior may emerge, including diffraction, tunneling, orbital quantization, and the emergence of wave-like statistics [1]. These rich and complex phenomena are far from being fully explored, warranting further study.

For a two-dimensional, monochromatic Faraday wave field, the mathematical model for the droplet's trajectory requires an integro-differential equation, rather than a temporally local differential equation, due to the hereditary nature of the pilot-wave system. This equation involves using a Bessel function as a wave kernel, which can make analysis unwieldy. By developing and exploring a one-dimensional model for the walking droplet dynamics, it is possible to more easily discover and rationalize new phenomena which also occur in the more complex model. To this end, the two-dimensional bath can be reduced to a single dimension, yielding a sinusoidal wave kernel, allowing significant reduction of complexity to a three-dimensional system for the particle's velocity and the wave evolution, parameterized by the strength of the vibrational forcing.

In this thesis, we briefly summarize the derivation of the one-dimensional pilot-wave model. We then analyze the linear stability of the walker's self-propulsion and show that chaos occurs beyond a subcritical Hopf bifurcation, whose form we compute. Finally, we provide computational evidence of a homoclinic bifurcation by studying the relationship between the vibrational acceleration and the period of the limit cycles arising from a subcritical Hopf bifurcation. The dynamics corresponding to this homoclinic bifurcations appear to provide a signature of the chaotic dynamics that arise at longer path memory.

2. Model Derivation

First, consider droplet-bath system in the case of the two-dimensional, monochromatic Faraday wave field. As described in Oza et al. [4], the position $\boldsymbol{x}_p(t) = (x_p(t), ,y_p(t))$ of a resonant walker in the period-doubled regime can be described by the following equation of motion:

$$m\ddot{\boldsymbol{x}}_p + D\dot{\boldsymbol{x}}_p = -\overline{F(t)\nabla h(\boldsymbol{x}_p, t)}, \tag{1}$$

where m is the droplet's mass, D is the drag coefficient, $F(t)$ is the applied forcing, h is the perturbation height of the fluid, and bar corresponds to the time average over one pouncing period T_F.

Assuming that Faraday waves dominate, the asymptotic form of the waves produced by the bouncing droplet

can be approximated by a Bessel function of the first kind. Additionally, assuming that the time scale of the droplet's horizontal motion is long compared to the bouncing period, we can average over the entire period, ignoring the drop's vertical motion. (This approximation is known as the *stroboscopic* approximation.) Using these assumptions, it can be shown that

$$
(2) \qquad m\ddot{\boldsymbol{x}} + D\dot{\boldsymbol{x}} = \frac{F}{T_F} \int_{-\infty}^{t} \frac{J_1(k_F|\boldsymbol{x}(t) - \boldsymbol{x}(s)|)}{|\boldsymbol{x}(t) - \boldsymbol{x}(s)|}(\boldsymbol{x}(t) - \boldsymbol{x}(s))e^{-(t-s)/(T_F M_e)}\mathrm{d}s
$$

Here, $T_F = 4\pi/\omega$ is the period of the droplet's vertical motion; $F = mgAk_F$ is a constant; and M_e is the dimensionless memory parameter. The term on the right indicates dependence on the droplet's entire path memory; all of the previous bounces affect the wave field which guides the droplet.

Equation 2 can be difficult to deal with, both analytically and numerically. We can simplify our model by assuming the fluid surface to be one-dimensional. Working in a parallel manner to Durey *et al.*, Equation 2 reduces to

$$
m\ddot{x}_p + D\dot{x} = -F_0 \frac{\partial h(x,t)}{\partial x},
$$

$$
(3) \qquad h(x,t) = \frac{A}{T} \int_{-\infty}^{t} \cos(k_F\, x_p(t) - x_p(s))e^{-(t-s)/\tau}\mathrm{d}s,
$$

where A is the stroboscopic amplitude of the wave generated by the droplet, k_F is the Faraday wavenumber and τ is the time scale over which waves decay. We non-dimensionalize by scaling lengths with k_F^{-1} and scaling time with the typical decay time $\tau_0 = \sqrt{DT_F/F_0 k_F}$, which we find to be the time at which sustained walking arises. We define the dimensionless mass as κ_0 and the dimensionless decay rate of waves as $\epsilon = \tau_0/\tau$. Later, we will often choose to refer to $\Gamma = 1 - \epsilon$, the path memory parameter, rather than ϵ itself. Using these, we obtain

$$
\kappa_0 \ddot{x}_p + \dot{x}_p = -h(x,t),
$$

$$
(4) \qquad h(x,t) = \int_{-\infty}^{t} \cos(x_p(t) - x_p(s))e^{-\epsilon(t-s)}\mathrm{d}s,
$$

where $h(x,t)$ is the dimensionless height of the perturbation of the wave field. Now, let $H(x,t)$ be the height of the wave field in the particle's frame of reference. Therefore, $H(x,t) = h(x + x_p(t), t)$. Defining $H(x,t) \equiv a(t)\cos(x) + b(t)\sin(x)$ and $v_p(t) \equiv \dot{x}$, we obtain the following three-dimensional system of differential equations:

$$
\kappa_0 \dot{v}_p + v_p + b = 0
$$

$$
(5) \qquad \dot{a} - v_p b + \epsilon a = 1
$$

$$
\dot{b} + v_p a + \epsilon b = 0
$$

In these differential equations, we see that each variable experiences damping forces. The velocity of the droplet is driven by b — the wave force increases with the wave's slope. The nonlinear terms are indicative of the frame of reference. Lastly, the 1 in the right-hand-side of the second equation drives a to increase — this represents how the droplet's impact on the fluid generates more waves.

3. Analysis at $\kappa_0 = 0$

We will now apply our model to the special case where $\kappa_0 = 0$. Since κ_0 is the dimensionless mass, this corresponds to the limit when inertial forces have only transient effects, with damping forces dominating the system in the long term. In this boundary case, the differential equations (5) simplify as follows:

$$
v_p + b = 0,
$$

$$
(6) \qquad \dot{a} - v_p b + \epsilon a = 1,
$$

$$
\dot{b} + v_p a + \epsilon b = 0.
$$

We can reduce to two dimensions by substituting for v_p. Rearranging for $\dot{a}$ and $\dot{b}$ gives

$$
\dot{a} = 1 - b^2 - \epsilon a,
$$

$$
(7) \qquad \dot{b} = ab - \epsilon b.
$$

Using the above, we can solve for the fixed points, which are

$$
a = 1/\epsilon \quad \text{and} \quad b = 0,
$$

$$
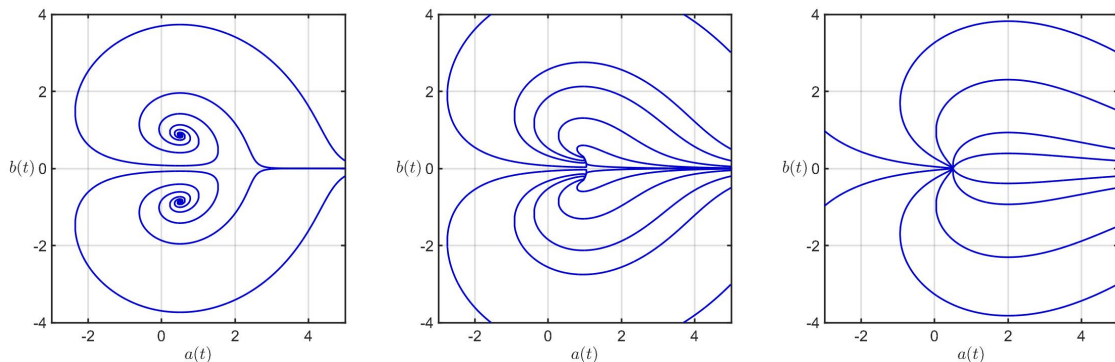(8) \qquad \text{or,} \quad a = \epsilon \quad \text{and} \quad b = \pm\sqrt{1 - \epsilon^2}.
$$

FIGURE 1. Characteristic trajectories of the $\kappa_0 = 0$ system. From left to right, the values of ϵ are 0.5, 0.95, and 2.0.

The first line corresponds to the bouncing state, while the second line corresponds to the two walking states, one for each direction. To determine the asymptotic linear stability of these states, we compute the Jacobian matrix

$$(9) \qquad \boldsymbol{J} = \begin{pmatrix} -\epsilon & -2b \\ b & a - \epsilon \end{pmatrix}.$$

For the fixed points, we have

$$(10) \qquad \begin{aligned} \boldsymbol{J}_{bouncing} &= \begin{pmatrix} -\epsilon & 0 \\ 0 & \frac{1}{\epsilon} - \epsilon \end{pmatrix}, \\ \boldsymbol{J}_{walking} &= \begin{pmatrix} -\epsilon & \mp 2\sqrt{1 - \epsilon^2} \\ \pm\sqrt{1 - \epsilon^2} & 0 \end{pmatrix}. \end{aligned}$$

To understand the asymptotic linear stability of these fixed points, we find the eigenvalues of the Jacobian matrices. In the bouncing case, we can simply read the eigenvalues from the diagonalized matrix. In the walking case, the quadratic formula yields:

$$(11) \qquad \lambda_{\pm} = \frac{-\epsilon \pm \sqrt{9\epsilon^2 - 8}}{2}.$$

For the bouncing state, one eigenvalue is always negative, and the other is negative only for $\epsilon > 1$. Thus, this fixed point is a saddle node for $0 < \epsilon < 1$ and is an attracting node for $\epsilon > 1$. For the walking state, the fixed point only exists for $0 < \epsilon < 1$. For $0 < \epsilon < \sqrt{\frac{8}{9}}$, the eigenvalue is complex with negative real part, yielding attracting spirals. For $\sqrt{\frac{8}{9}} < \epsilon < 1$, both eigenvalues are real and negative, so the walking states are attracting nodes.

Does this overdamped system exhibit any closed orbits, in addition to these fixed points? We show this is not the case using Dulac's Criterion [5].

Theorem 3.1. *Dulac's Criterion. Let $\dot{\boldsymbol{x}} = \boldsymbol{f}(\boldsymbol{x})$ be a continuously differentiable vector field on a simply-connected subset R of the plane. If there exists a continuously differentiable, real-valued function $g(\boldsymbol{x})$ such that $\nabla \cdot (g(\boldsymbol{x})\dot{\boldsymbol{x}})$ has one sign throughout R, then there are no closed orbits lying entirely in R.*

We apply this criterion to Equation 7, using $g(\boldsymbol{x}) = b^{-1}$. Since $\nabla \cdot (g(\boldsymbol{x})\dot{\boldsymbol{x}}) = -\epsilon/b$, the conditions are satisfied if we define R as $\{\boldsymbol{x} \in R_1 \,|\, b > 0\}$ or as $\{\boldsymbol{x} \in R_2 \,|\, b < 0\}$. Furthermore, there are no trajectories that exist in both regions because no trajectory can cross the nullcline $b = 0$. Therefore, there exist no closed orbits.

How do we interpret these findings? When the dimensionless decay rate ϵ is large, waves decay too rapidly for wave memory to have a strong effect, so the droplet's stable equilibrium is at the peak of a wave. However, once $\epsilon < 1$, the dimensionless decay rate is low enough for the pilot-wave memory to break the symmetry of the system, resulting in stable motion to either the left or right.

4. Regime Diagram

Having discussed the stability of the system when $\kappa_0 = 0$, let us now generalize the analysis to the case $\kappa_0 > 0$. To calculate the fixed points, we use Equation 5 and set the derivatives equal to zero:

$$\begin{aligned} v_p + b &= 0, \\ -v_p b + \epsilon a &= 1, \\ v_p a + \epsilon b &= 0. \end{aligned}$$

(12)

Again making use of substitution for v_p, we find three fixed points:

$$v_p = 0, \quad a = 1/\epsilon \quad \text{and} \quad b = 0,$$

(13)

$$\text{or,} \quad v_p = \pm\sqrt{1 - \epsilon^2}, \quad a = \epsilon \quad \text{and} \quad b = \mp\sqrt{1 - \epsilon^2}.$$

As with the case $\kappa_0 = 0$, these fixed points correspond to the bouncing and walking states, respectively. The Jacobian can be calculated directly from Equation 5:

$$\boldsymbol{J} = \begin{pmatrix} -1/\kappa_0 & 0 & -1/\kappa_0 \\ b & -\epsilon & v \\ -a & -v & -\epsilon \end{pmatrix},$$

(14)

from which we may infer the asymptotic linear stability of these two dynamical states. The eigenvalues of the walking state, which is the main focus of this study, are thus roots of the characteristic polynomial:

(15)
$$\kappa_0 \lambda^3 + \lambda^2(1 + 2\kappa_0\epsilon) + \lambda(\kappa_0 + \epsilon) + 2(1 - \epsilon^2) = 0.$$

4.1. **Boundary of Instability.** The boundary at which the steady walking state becomes unstable can be calculated analytically. Unstable oscillations occur when a complex eigenvalue begins to have positive real part. Therefore, at the boundary of instability, there are a pair of conjugate imaginary eigenvalues $\pm i\omega_c$. After substituting $\lambda = i\omega_c$ into Equation 15, we can separate the real and imaginary parts to get two equations:

$$\begin{aligned} \omega_c^2 &= 1 + \frac{\epsilon_c}{\kappa_0}, \\ \omega_c^2(1 + 2\kappa_0\epsilon_c) + 2(1 - \epsilon_c^2) &= 0. \end{aligned}$$

(16)

By eliminating ω_c and solving for ϵ_c in terms of κ_0, we obtain a quadratic polynomial for ϵ_c. We find that one root of this polynomial is positive for all $\kappa_0 > 0$, and the other is negative. As the physical problem requires $\epsilon_c > 0$ we deduce that

(17)
$$\epsilon_c = \frac{-1 - 2\kappa_0^2 + \sqrt{(2\kappa_0^2 + 1)^2 + 16\kappa_0^2}}{8\kappa_0}.$$

4.2. **Boundaries of Critical Damping and Subdominant Oscillations.** The boundaries marking the onset of critical damping and subdominant oscillations are less easy to study analytically for this system. Instead, we calculate them numerically from the cubic polynomial 15. Critical damping occurs when a complex pair of eigenvalues collide, and subdominant oscillations occur when the real part of the complex pair of eigenvalues exceeds that of the third eigenvalue. We iterated over values of κ_0 and ϵ_0 computationally to plot these two curves (Figure 2). The results are strikingly similar to those of Durey *et al.*, indicating that changing the form of the wave kernel does not modeify the qualitative features of the system.

4.3. **Limit for Small κ_0.** As we derived previously, instability occurs when $\epsilon = 0$. Critical damping occurs at $\epsilon = \sqrt{\frac{8}{9}}$. Both of these findings agree graphically with Figure 2.

4.4. **Limit for Large κ_0.** To calculate the behavior of the boundary of instability at large κ_0, we can start by factoring out κ_0^2 from Equation 17, yielding

(18)
$$\epsilon_c = \left(-\left(\frac{1}{\kappa_0^2} + 2 \right) + \sqrt{\left(\frac{1}{\kappa_0^2} + 2 \right)^2 + \frac{16}{\kappa_0^2}} \right) \left(\frac{\kappa_0}{8} \right).$$

Using a Maclaurin series and neglecting higher order terms, we have that

(19)
$$\epsilon_c \approx \frac{1}{2\kappa_0}.$$

We thus conclude that the walking state destabilizes for all $\kappa_0 > 0$ for sufficiently large vibrational forcing.
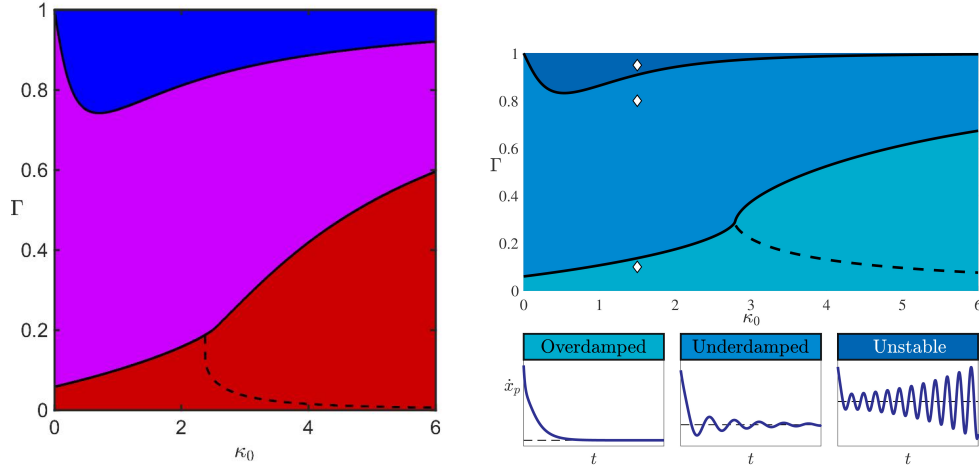
FIGURE 2. *Left:* Regime diagram showing the linear stability of the walking state fixed points. From bottom to top, the colored regions represent overdamped, underdamped, and unstable oscillations in phase space. The dashed line indicates the onset of subdominant oscillations. *Right:* The analogous figure made by Durey *et al.* for the two-dimensional, monochromatic Faraday wave field, shown here for comparison. The qualitative features are identical, lending credence to the predictions of our reduced one-dimensional model.

5. HOMOCLINIC BIFURCATION

The instability threshold appears to correspond to a subcritical Hopf bifurcation because small limit cycles do not appear for $\Gamma > \Gamma_c$. Instead, the dynamics head to a distant, chaotic attractor. Knowing this, we choose instead to investigate the homoclinic bifurcation at $\Gamma_h < \Gamma_c$. A homoclinic bifurcation is an infinite-period bifurcation that occurs when a limit cycle collides with a saddle [5]. If we let μ be a dimensionless measure of the distance between the limit cycle and the bifurcation, the orbital period T will exhibit a logarithmic scaling with respect to μ.

$$T \sim O(|\log \mu|) \tag{20}$$

5.1. **Justification of Logarithmic Scaling Law.**
To demonstrate the intuition behind this scaling law, consider a limit cycle that passes near a saddle node. The trajectory moves slowly near the saddle node, so the dominant contribution to T occurs in this neighborhood. Near the saddle, we can make a linear approximation of the trajectory. For the purposes of demonstrate, we take the following as an example of such an approximation:

$$\begin{aligned} \dot{x} &= y \\ \dot{y} &= -x \end{aligned} \tag{21}$$

Suppose the limit cycle approaches the saddle from the right. To estimate the orbital period, we can estimate the amount of time it takes for the trajectory to pass between two arbitrary boundaries sufficiently near the saddle — for instance, between $y = -Y$ and $y = Y$. The solution for $y(t)$ from Equation 21 is

$$y(t) = C_1 e^t + C_2 e^{-t}. \tag{22}$$

At $t = 0$, consider $x = \mu$ and $y = 0$. This implies that

$$y(t) = \frac{\mu}{2}(e^t + e^{-t}). \tag{23}$$

For $\mu \ll Y$, the travel time between $-Y$ and Y is

$$T \approx 2\log(2Y) - 2\log\mu. \tag{24}$$

Since Y is $O(1)$, we have our scaling law (Equation 20).

5.2. **Fourier Series Approximation of Limit Cycles Using Newton's Method.**
In order to find periodic solutions for $\Gamma < \Gamma_c$, we define the Fourier transform of a periodic function $f(t)$ with period T as

$$\hat{f}_n = \mathfrak{F}[f(t)] \equiv \frac{1}{T}\int_0^T f(t)e^{-in\omega t}\mathrm{d}t \tag{25}$$

and its inverse as

$$(26) \qquad f = \mathfrak{F}^{-1}[\hat{f}_n](t) \equiv \sum_{n=-\infty}^{\infty} \hat{f}_n e^{in\omega t},$$

where $\omega = 2\pi/T$ is the angular frequency. If we apply the forward transform to Equation 5 and use the convolution theorem when $\mathfrak{F}$ is applied to products, we obtain the following system of equations for all integers n:

$$(27) \qquad \begin{aligned} (1 + in\omega\kappa_0)\hat{v}_n + \hat{b}_n &= 0, \\ (\epsilon + in\omega)\hat{a}_n - \sum_{m=-\infty}^{\infty} \hat{v}_m \hat{b}_{n-m} &= \delta_{n0}, \\ (\epsilon + in\omega)\hat{b}_n - \sum_{m=-\infty}^{\infty} \hat{v}_m \hat{a}_{n-m} &= 0, \end{aligned}$$

with $\hat{v}_n$, $\hat{a}_n$, and $\hat{b}_n$, being the Fourier coefficients of the corresponding variables, and δ_{nm} being the Kronecker Delta. Eliminating $\hat{b}_n$ and performing an index shift, we get

$$(28) \qquad \begin{aligned} (\epsilon + in\omega)\hat{a}_n + \sum_{m=-\infty}^{\infty} (1 + im\omega\kappa_0)\hat{v}_m \hat{v}_{n-m} &= \delta_{n0}, \\ (\epsilon + in\omega)(1 + in\omega\kappa_0)\hat{v}_n - \sum_{m=-\infty}^{\infty} \hat{v}_m \hat{a}_{n-m} &= 0. \end{aligned}$$

Lastly, to guarantee a unique limit cycle, due to temporal invariance, we choose to seek limit cycles that satisfy $\dot{v}_p(0) = 0$, giving us our last equation:

$$(29) \qquad \sum_{n=-\infty}^{\infty} n\hat{v}_n = 0.$$

To execute the numerical study, we truncated the system for high frequencies. Specifically, we specified N and took $\hat{a}_n = \hat{v}_n = 0$ for $|n| > N$. (In this paper, we used $N = 80$.) Then, we treated Γ as a known independent variable and T, $\hat{a}_n$, and $\hat{v}_n$ as the $4N + 3$ unknowns. Using Newton's Method with an error tolerance of 10^{-10}, we calculated these unknowns for $0.2 < \kappa_0 < 6$, iterating until the T exceeded 150. To evaluate the validity of the truncation of high frequencies, we evaluated the maximum absolute value of $\hat{v}_{\pm N}$ and $\hat{a}_{\pm N}$. This value exceeded 0.1 at most once for each given value of κ_0 (out of dozens of simulations with different values of Γ); typically, the value was much smaller, and also tended to grow smaller as κ_0 increased.

5.3. **Curve Fitting Provides Evidence of a Homoclinic Bifurcation.** After generating data regarding the relationship between T, Γ, and κ_0, we fitted the data to the logarithmic curve $A\log(B - \epsilon) + C$ in order to calculate Γ_h, the critical value at which the homoclinic bifurcation occurs; Γ_h typically had confidence bounds within 1% of the estimated value. The results are plotted below for $0.2 < \kappa_0 < 6.0$. Further studies could investigate the behavior for $\kappa_0 \to 0$ and $\kappa_0 \to \infty$.

5.4. **Subcritical Hopf Bifurcation.** Using the same data generation method, we can also provide evidence of a subcritical Hopf bifurcation at the boundary of instability (see Figure 4).

6. Conclusion

The walking droplet problem brings with it a host of fascinating phenomena to study and model. In order to facilitate this research, we sought to define analyze the analogous problem with a one-dimensional fluid surface, reducing the problem to three dimensions. After analyzing the linear stability of this system, we utilized Fourier transforms, Newton's Method, and a logarithmic scaling law to provide evidence of a both a homoclinic bifurcation and a subcritical Hopf bifurcation. The similarities between the results of this one-dimensional system and the results found by Durey *et al.* for the two-dimensional system helps support the notion that the one-dimensional system can be useful as a predictive tool. The existence of the homoclinic bifurcation hints at the possible chaotic behaviors at $\Gamma > \Gamma_c$. Indeed, simply plotting the trajectories in v-a-b-space suggests the existence of a strange attractor. Future studies could investigate the unstable region of the regime diagram, mapping out the onset of various behaviors — such as strange attractors, limping modes, etc. Perhaps in analyzing this simpler system, other researchers will discover phenomena not yet discovered in the two-dimensional model.
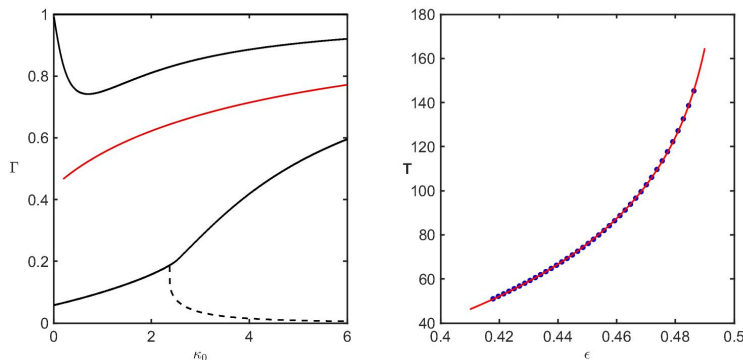
FIGURE 3. *Left:* In red, a plot of Γ_h, derived by fitting T and Γ to a logarithmic relationship. In black, the same data as in Figure 2, for reference. *Right:* An example of the agreement of the fitted curve and the raw data. For clarity, only one sixth of the data points are shown. The fit was computed with $\kappa_0 = 0.5$ and with $N = 80$ Fourier modes. The resulting model was $T = -48.9 \log(0.4978 - \epsilon) - 72.8$, corresponding to $\Gamma_h = 0.5022 \pm 0.0001$.
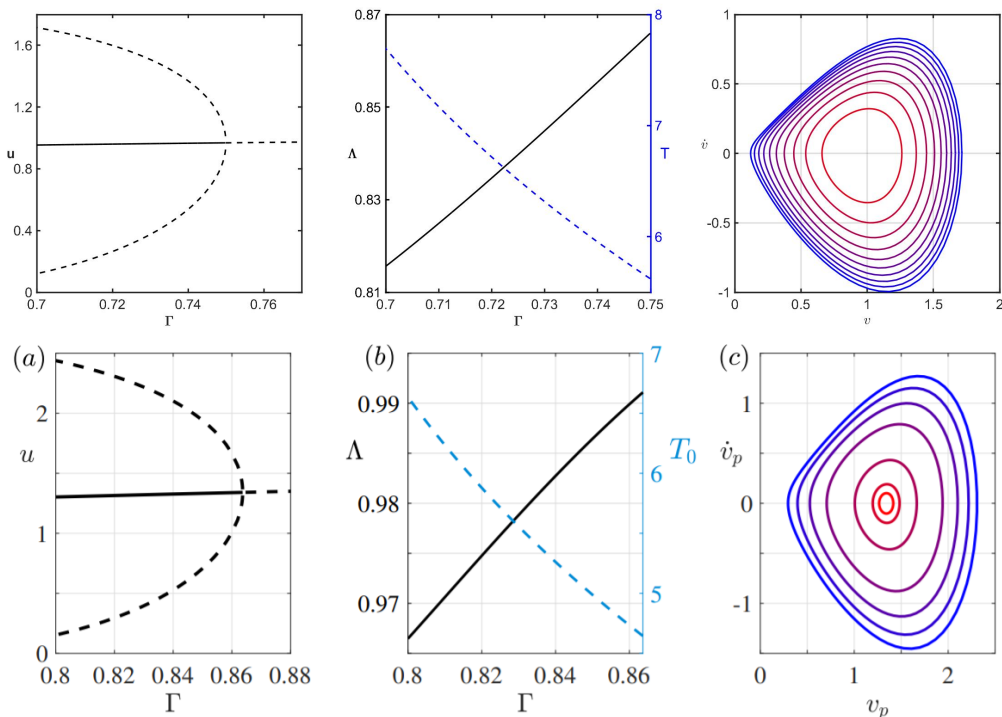

FIGURE 4. *Top left:* The stable dimensionless walking speed plotted (solid curve) and the velocity bounds of the unstable limit cycle (dashed) plotted against Γ for $\kappa_0 = 1$, with $\Gamma_c = 0.75$. *Top middle* The relative oscillation length Λ (black) and dimensionless oscillation period T_0 (blue). *Top Right:* Some sample limit cycles for values of Γ between 0.7 (red) and 0.75 (blue). *Bottom:* The analogous figure made by Durey *et al.* for the two-dimensional, monochromatic Faraday wave field, shown here for comparison. Like in Figure 2, the qualitative features are identical.

7. ACKNOWLEDGEMENTS
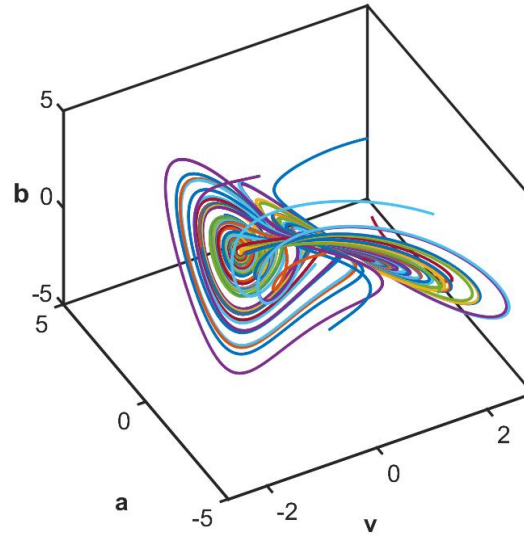
Strange

FIGURE 5. A strange attractor. $\kappa_0 = 1$, $\Gamma = 0.9$.

REFERENCES

1. John W. M. Bush, *Pilot-wave hydrodynamics*, Annu. Rev. Fluid Mech. **47** (2015), 2269–288.
2. Y. Couder, S. Protière, E. Fort, and A. Boudaoud, *Walking and orbiting droplets*, Nature **437** (2005).
3. M. Durey, S. E. Turton, and J. W. M. Bush, *Speed oscillations in classical pilot-wave dynamics*, Proc. Roy. Soc. A (2020), 3–6, 8–11, Under review.
4. A. U. Oza, R. R. Rosales, and J. W. M. Bush, *A trajectory equation for walking droplets: hydrodynamic pilot-wave theory*, J. Fluid Mech.: 2013 **737** (2013), 555–558.
5. Steven H. Strogatz, *Nonlinear dynamics and chaos*, Westview Press, 2015.